Bandgap Fluctuations, Hot Carriers, and Band-to-Acceptor Recombination in $Cu_2ZnSn(S,Se)_4$ Microcrystals

Jüri Krustok,* Reelika Kaupmees, Nafiseh Abbasi, Katri Muska, Idil Mengü, and Kristi Timmo

Temperature and laser power dependencies of the band-to-acceptor recombination in $Cu_2ZnSn(S_xSe_{1-x})_4$ ($x = 0.7$) microcrystals, which exhibit large bandgap energy fluctuations, are studied. The average depth of these fluctuations is approximately 79 meV. The shape of the corresponding wide photoluminescence (PL) band is analyzed using a modified localized-state ensemble model. The temperature dependence of this PL band is demonstrated to be influenced by the redistribution of holes between potential wells in the valence band with varying depths. The shape of this band at different temperatures is well fitted when an effective carrier temperature is introduced. This temperature is found to be approximately 300 K higher than the lattice temperature in the samples, and it is mainly caused by the very short minority carrier lifetime. According to the laser power-dependent PL studies, there is a consistent reduction in the effective carrier temperature as the laser power increases. This phenomenon is explained by the dominance of nonradiative Shockley–Read–Hall recombination at lower temperatures.

1. Introduction

Although it has been an active area of research for over half a century, the development of new materials for solar energy harvesting is currently a major focus in the renewable energy field. Kesterite $Cu_2ZnSn(S,Se)_4$ (CZTSSe) materials have emerged as a promising contender for widespread photovoltaic deployment in the future. These materials are made from nontoxic, earth-abundant components. Furthermore, they have excellent optoelectronic properties, making them highly suitable for achieving high power conversion efficiency.[1] Despite the increasing amount of research, the open-circuit voltage (V_{OC}) characteristics of the top-performing kesterite solar cells only reach 60% of the maximum value possible.[2] The primary causes for this significant deficit in V_{OC} are believed to be carrier recombination in the bulk and a high recombination rate at the interface between the absorber and buffer layers. Further research is required to gain a better understanding of the recombination

mechanisms present in kesterite compounds. Photoluminescence (PL) spectroscopy is frequently utilized to identify various defects and recombination processes. PL properties of kesterite materials are usually determined by a high concentration of charged intrinsic point defects. These uncompensated point defects give rise to electrostatic potential fluctuations, and, as a result, new recombination channels appear. They are related to valence and conduction band tail states. Moreover, potential fluctuations are responsible for spreading out defect levels inside of bandgap. Therefore, we can expect band-to-band (BB), band-to-tail (BT), and band-to-acceptor (BI) recombinations in these materials. In kesterites the small effective mass of electrons ($m_e/m_0 = 0.18$) compared with the high effective mass of holes ($m_p/m_0 = 2$)[3] creates a situation, where electrons are typically not localized inside potential wells created by charged defects or bandgap fluctuations and the distribution of holes between localized valence band tail states determines properties of PL bands.[4] All these recombinations were studied by Levanyuk and Osipov.[4] Later, it was shown that BI, BT, and BB recombinations are present in chalcopyrites[5–7] and also in kesterites like $Cu_2ZnSn(S,Se)_4$.[8–11] The observed low-temperature wide PL bands have an asymmetrical shape; the peak position exhibits a rapid redshift with temperature having a minimum value at around $T = 100–200$ K. With increasing laser power, the peak position shows a blueshift in the range of 10–20 meV per decade. All of these characteristics are observable in chalcopyrites. However, kesterites demonstrate extra Gaussian bandgap energy fluctuations, which are caused by differences in the spatial degree of Cu–Zn ordering, localized clusters of defects, or variations in composition. It is known that CZTSSe crystallizes in the disordered kesterite structure, where the $2d$ Wyckoff positions of the (001) cationic planes are randomly occupied by Cu and Zn atoms. The so-called ordered–disordered transition in CZTS and in CZTSe happens at $T = 260\,°C$ and $T = 200\,°C$, respectively.[12] Low-temperature ordered phase can have about 100 meV higher bandgap energy than the high-temperature disordered phase.[13] Simultaneous presence of both phases results in a double PL band structure with abnormally wide full width at half maximum (FWHM) of an aggregate band.[14] The disordered phase with a lower bandgap energy inside the mostly ordered lattice can create potential wells also for electrons initializing additional

J. Krustok, R. Kaupmees, N. Abbasi, K. Muska, I. Mengü, K. Timmo
Department of Materials and Environmental Technology
Tallinn University of Technology
Ehitajate tee 5, 19086 Tallinn, Estonia
E-mail: juri.krustok@ttu.ee

tail-to-acceptor (TI) and tail-to-tail (TT) recombinations. As it was mentioned before, various defect clusters are also responsible for bandgap fluctuations, and rather deep potential wells for both holes and electrons can be found in kesterites.[15–17] It is proposed that these defect clusters are the main source of the kesterite band tails and bandgap energy fluctuations.[18]

The most common PL band in kesterites is a BI band. The theoretical model for the BI band was first introduced by Levanyuk and Osipov.[4] Later this model was improved by Jagomägi et al.[19] Unfortunately, all these models fail to describe the shape and temperature dependence of the BI band in cases of strong bandgap fluctuations. In this study, we will perform a detailed analysis of BI recombination in CZTSSe crystals with strong bandgap fluctuations.

2. Result and Discussion

The temperature dependence of the PL band in our CZTSSe sample is presented in **Figure 1**a.

The low-energy (LE) side of the wide PL band shows a Gaussian shape and the peak position displays a visible redshift with increasing temperature. Moreover, the PL band at low temperature has an asymmetric shape with a steeper decline on the high-energy (HE) side. It was shown previously in many articles[6,20–22] that the LE side of these asymmetric PL bands at low temperatures is more or less determined by the density of states function $\rho(E)$ while the temperature-dependent distribution function $f(E)$ controls the shape of the HE side of the PL band. A Gaussian density of states function is typical

for defect-related emission (BI) and for BT emission usually exponential shape is detected.[23] The PL band integral intensity Φ decreases with temperature according to the simple exponential law[24]

$$\Phi(T) = \Phi_0/[1 + \alpha_1 T^{3/2} + \alpha_2 T^{3/2} \exp(-E_A/kT)] \quad (1)$$

where Φ is the integrated intensity of the PL band, α_1 and α_2 are the process rate parameters, and E_A is the thermal activation energy (see Figure 1b. The calculated thermal activation energy $E_A = 121 \pm 8$ meV indicates that quite deep acceptor defects are involved in PL emission. The most probable defect having an activation energy in this range is the Cu_{Zn} acceptor defect.[12] Hence, we expect BI type of recombination where the occupation of acceptor levels is determined by the localized holes inside potential wells created by bandgap and/or potential fluctuations and electrons can be considered as free. It should be mentioned that at suitable temperatures and deeper bandgap fluctuations, it is possible that also electrons can localize inside potential wells created at the edge of the conduction band. The distribution of holes between potential wells with different depths is mostly determined by the temperature. At very low temperatures, holes will typically occupy shallow wells and thus giving rise to the HE part of the BI band. Increasing temperature leads to redistribution holes from shallow wells into deeper ones, and the corresponding emission band will shift toward LE (see **Figure 2**).

At higher temperatures, the PL band starts to blueshift because all localized holes are liberated and we are dealing with capturing free holes from the valence band into acceptor defect
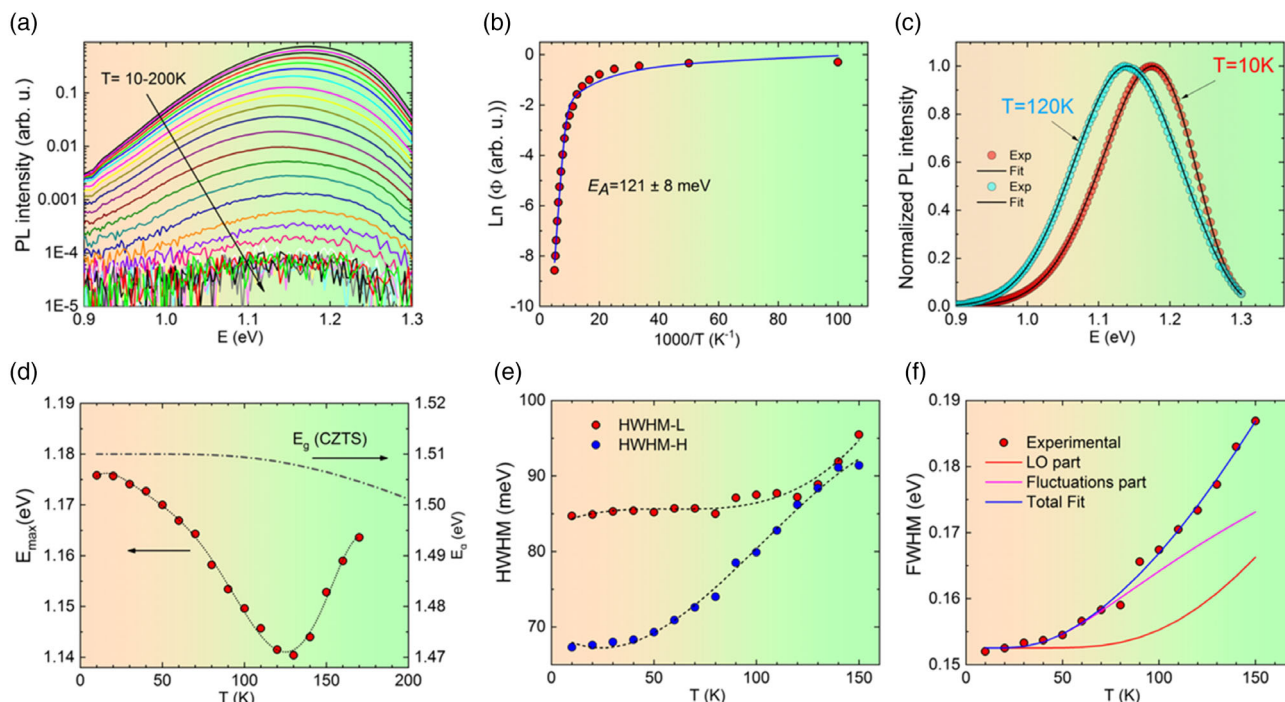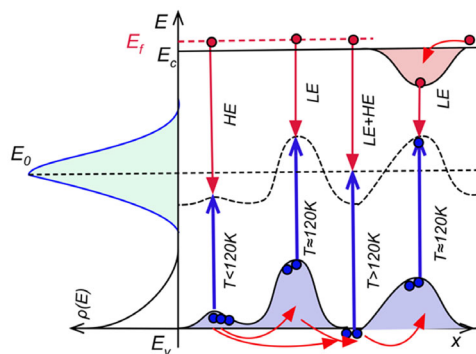

Figure 1. a) Temperature dependence of PL emission from CZTSSe microcrystals, b) thermal quenching of integral intensity Φ and fitting using Equation (1) (solid line), c) example of spectral fitting with Equation (2) for two different temperatures, d) temperature dependence of PL peak maximum E_{max} and bandgap energy of CZTS,[38] e) temperature dependence of HWHM values for low- and high-energy sides of the PL band, and f) temperature dependence of FWHM and result of fitting using Equation (3).

states. The distribution of holes between these localized states is affecting the shape and temperature dependence of the PL band. Similar situations were analyzed in different articles[20,25,26] by using the following simplified and modified localized-state ensemble (LSE) model

$$I(E) \propto \rho(E)f(E) \propto \exp\left[-\frac{(E-E_0)^2}{2\sigma^2}\right] * \frac{1}{\exp\left(\frac{E-E_a^*}{kT_e^*}\right) + \tau_{tr}/\tau_r} \quad (2)$$

where E_0 is a peak position and σ is the standard deviation of the distribution function of acceptor states, E_a^* is a "marking" level below which all the localized states are occupied by carriers (analogously to a quasi-Fermi level), and T_e^* is an effective carrier temperature. It should be mentioned that in the original LSE model[26] proposed for quantum dots the lattice temperature T was implemented. However, in order to fit the experimentally measured PL band shape, the effective carrier temperature T_e^* must be used. Although, in principle, a carrier temperature could be extracted from the HE tail of the PL band, increasing the lattice temperature also results in phonon-related broadening of the PL spectra. Also, the role of bandgap fluctuations increases with the depth of these fluctuations. Therefore, the extracted carrier temperature from PL spectra is usually higher than the real carrier temperature, and the difference is bigger at higher temperatures. Accordingly, the term "effective carrier temperature" was used here. At $T = 10$ K, $\sigma = 79$ meV and this value can be considered as the average amplitude of fluctuations. The average depth of electrostatic potential fluctuations in CZTSSe usually does not exceed 50 meV[27] and therefore we expect that bandgap fluctuations are dominant in our sample. The term $1/\tau_r$ represents the rate of radiative recombination, while $1/\tau_{tr}$ is the attempt-to-escape rate of the localized carriers. An analysis of Equation (2) shows that the shape of the HE tail is mainly determined by T_e^* while E_a^* and τ_{tr}/τ_r control the expanse of the distribution (see Figure S4, Supporting Information). Examples of the fittings with Equation (2) for $T = 10$ K and $T = 120$ K spectra are given in Figure 1c. The peak position of the PL band E_{max} shows quite rapid redshift with temperature and reaches a minimum value at $T = 130$ K. At $T > 130$ K, the peak position value starts to increase again (see Figure 1d. The rate of this redshift at low temperatures exceeds the rate of bandgap energy E_g dependence shown for CZTS in Figure 1d. We assume that the $E_g(T)$ dependence in our CZTSSe samples has quite similar rate.

The temperature dependence of the half width at half maximum for HE and LE sides (HWHM-H and HWHM-L) is given in Figure 1e. As expected, the HWHM-L shows only a very small increase because of temperature independent $\rho(E)$ function at low temperatures while the HWHM-H is rapidly growing with temperature because of electron–phonon interaction and variation of T_e^* value. At about $T = 120$ K, the PL band has a symmetrical Gaussian shape. We also investigated the temperature dependence of FWHM (see Figure 1f. The FWHM value shows an unusually rapid increase with temperature that is not typical for pure electron–phonon interaction, and therefore we expect bandgap fluctuations to also contribute through effective carrier temperature T_e^*. The origin of FWHM behavior as a function of temperature in this case can be determined based on a model first presented by Lee et al.,[28] The total linewidth of the PL spectrum is given by
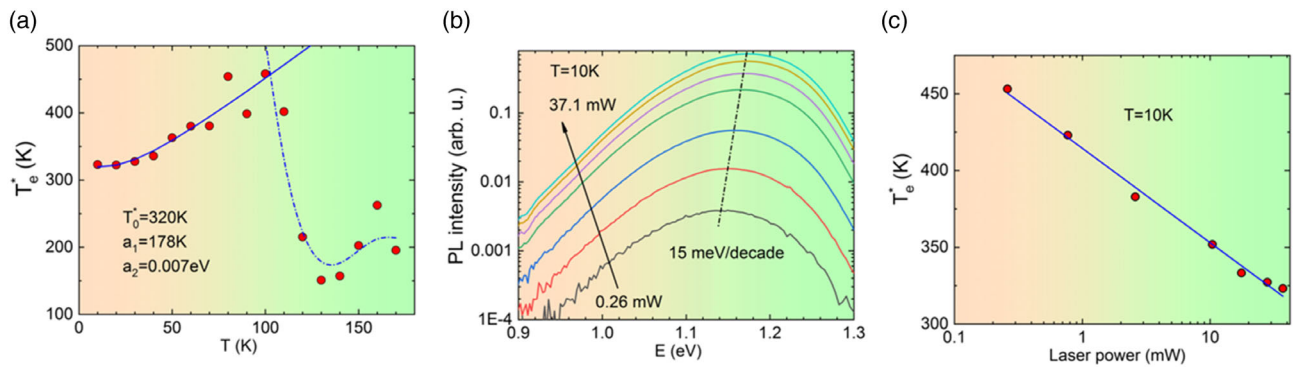
$$\text{FWHM}(T) = W_0 + \frac{W_1}{\left[\exp\left(\frac{\hbar\omega_{LO}}{kT}\right) - 1\right]} + W_2\exp(-E_{fl}/kT) \quad (3)$$

where W_0 denotes the width at $T = 0$ K including also inhomogeneous broadening, the second term represents the interaction with optical phonons, $\hbar\omega_{LO}$ is the LO-phonon energy ($\hbar\omega_{LO} = 41$ meV for CZTS was used),[29] and the last term represents how much fluctuations in the system can expand the linewidth of the PL spectra. The E_{fl} can be thought of as the average depth of shallow potential wells, which, as temperature rises, will be emptied, increasing the significance of deeper wells and, consequently, widening the PL band by widening the energy distribution of potential wells with different depth. We skipped an interaction with acoustic phonons because it is usually very weak. The result of the fitting with both components is given in Figure 1f where LO-phonon energy was fixed during fitting. The value of $E_{fl} = 14.8$ meV. Very similar energy values were obtained in ref. [30] as well.

The concept of the effective carrier temperature indicates that, although the energy distribution of charge carriers can be described by the Fermi–Dirac distribution, the effective carrier temperature T_e^* is higher than the lattice temperature T. The different temperatures of the carriers and the lattice are a natural outcome of the relatively short photocarrier lifetime τ, i.e., $T_e^* \sim \tau^{-1}$.[31,32] If a minority carrier lifetime is very short, excited carriers with high temperatures will recombine before they can "cool down" to lattice temperature T as a result of carrier–phonon interaction and carrier–carrier scattering. It is known that in kesterite compounds, the actual lifetime of the photoexcited carriers is extremely small and does not exceed values of hundreds of picoseconds.[12,33] Therefore, we also expect quite high T_e^* values. The temperature dependence of T_e^* is given in **Figure 3**a. At low temperatures, the effective carrier temperature increases as

$$T_e^*(T) = T_0^* + a_1/[\exp(a_2/kT) - 1] \quad (4)$$

where T_0^*, a_1, and a_2 are the fitting parameters. The increase of T_e^* corresponds to a decrease of τ with temperature, and this

Figure 2. Recombination model for the BI band in CZTSSe microcrystals with strong bandgap energy fluctuations. Note that deeper potential wells for holes (and also for electrons) affect mostly the LE side of the PL band, while shallow wells contribute to the HE side. The redistribution of holes between potential wells causes both redshift and blueshift of the PL band with increasing temperature.

Figure 3. a) Temperature dependence of an effective carrier temperature T_e^* and fitting result with Equation (4); b) PL spectra measured at $T = 10$ K using different laser powers. PL peak position shows a blueshift of 15 meV per decade of laser power; c) laser power dependence of T_e^*.

behavior is typical for different recombinations. At $T = 110$ K, the T_e^* shows a rapid drop, indicating a change in the recombination process. Indeed, in this temperature region, all localized holes are liberated, and the capture of holes by acceptor levels will be different.

Figure 3b presents the laser power dependence of the PL spectrum of CZTSSe measured at $T = 10$ K. The peak position of the PL band shows a blueshift of 15 meV per decade of laser power. This blueshift is quite typical for semiconductor materials with potential and/or bandgap fluctuations. The blueshift in our case can be attributed to the band filling effect and/or effect of decreasing of T_e^* with laser power. Indeed, Figure 3c shows a constant decease of T_e^* corresponding to an increase of carrier lifetime τ with increasing laser power. It is known that different types of nonradiative and radiative recombinations have also a different carrier lifetime dependence on laser power (see, e.g., ref. [34]) Usually, the effective minority carrier lifetime is determined by a combination of recombination rates

$$\frac{1}{\tau} = \frac{1}{\tau_{rad}} + \frac{1}{\tau_{Aug}} + \frac{1}{\tau_{SRH}} \tag{5}$$

where τ_{rad} is a radiative recombination lifetime, τ_{Aug} is a lifetime related to Auger recombination, and τ_{SRH} is a defect-related Shockley–Read–Hall (SRH) recombination lifetime. The SRH recombination was studied in a classical work[35] and it was shown that the minority carrier lifetime caused by SRH recombination increases in certain conditions with excess carrier concentration, i.e., with increasing laser power. For other recombinations, the lifetime usually decreases with laser power.[34] Consequently, the decrease of T_e^* with laser power is related to nonradiative SRH recombination dominating at low temperatures.

3. Conclusion

In conclusion, we conducted a PL study on CZTSSe microcrystals with large bandgap energy fluctuations in the temperature range of 10–200 K. We demonstrated that the PL band arises from band-to-acceptor recombination, and the depth of the acceptor defect was determined to be 121 meV. The shape and temperature dependence of this PL band were analyzed using a modified localized-state ensemble model, which employed

an effective carrier temperature T_e^* in place of the lattice temperature T. Our analysis showed that T_e^* rapidly decreased at $T = 110$ K, indicating a transformation in the recombination process. Furthermore, it was noted that there was a decrease in T_e^* as the laser power increased, which was linked to the prevalence of nonradiative SRH recombination at low temperatures.

4. Experimental Section

The CZTSSe microcrystals used in this study were synthesized by the molten salt (flux material) synthesis-growth method. As precursors, Cu powder (99.999%, Alfa Aesar), Sn shots (99.999%, Alfa Aesar), ZnS powder (99.999%, Alfa Aesar), S pieces (99.999%, Alfa Aesar), and Se shots (99.999%, Alfa Aesar) were used. As flux material, water-soluble potassium iodide with the mass ratio of liquid KI to solid CZTSSe of 1.2:1 (g/g) was used. The precursors with the intended initial composition of $Cu_{1.914}Zn_{1.08}Sn_{0.982}S_{2.68}Se_{1.32}$ and KI were weighed in desired amounts and ratios, loaded into a quartz ampoule, and mixed by shaking. The filled ampoule was degassed under a dynamic vacuum, sealed, and heated isothermally at 740 °C for 110 h. After cooling the ampoule to room temperature, the flux material was removed from the batch by leaching and rinsing with distilled water. The released microcrystal powder was dried in a hot-air oven at 50 °C and sieved into several narrow granulometric fractions between 38 and 125 μm. More details about the growth process of kesterite-based microcrystal powder can be found in ref. [36]. After synthesis, the powder was etched with 0.1 vol% Br in methanol for 60 s and with 10 wt% KCN aqueous solution for 90 s at room temperature, and afterward annealed isothermally in a vacuumed ampoule (volume ≈2 cm³) at 740 °C 35 min. Then, the furnace was switched off until the ampoule reached room temperature. The composition of the main constituent elements in the CZTSSe powder crystals was analyzed by energy-dispersive X-ray spectroscopy (EDX) on HR-SEM Zeiss Merlin equipped with Bruker EDX-XFlash6/30 detector with an accelerating voltage of 20 kV. According to the EDX analysis, the postannealed CZTSSe crystals had an average composition of $Cu_{1.95}Zn_{1.03}Sn_{1.04}S_{2.81}Se_{1.19}$. Composition $[S]/([S] + [Se]) = 0.7$ was used to reduce the bandgap energy for a better match with solar spectrum. The room temperature bandgap energy for this composition is estimated to be near 1.4 eV.[37] The average size of used CZTSSe microcrystals was about 63–75 μm (see Figure S1, Supporting Information). The elemental composition of different crystals showed small fluctuations (see Figure S2, Supporting Information). Phase purity of CZTSSe powder crystals was verified by micro-Raman spectroscopy using Horiba's LabRam HR 800 spectrometer equipped with a cooled multichannel CCD detector in the backscattering configuration and a 532 nm laser line. Raman spectroscopy measurements verified the presence of the CZTSSe phase (see Figure S3, Supporting Information); no other phases were detected.

A 0.64 m focal length single grating (600 mm^{-1}) monochromator and the 442 nm line of a He–Cd laser with different powers were used for PL measurements. For PL signal detection, a Hamamatsu InGaAs photomultiplier tube (PMT) was used. A closed-cycle helium cryostat (Janis CCS-150) was employed to measure temperature dependencies of the PL spectra at temperatures from 10 to 200 K. More than 100 microcrystals were excited during the PL measurements using a laser spot with a diameter of 700 µm (maximum power density was 9 W cm^{-2}).

Supporting Information

Supporting Information is available from the Wiley Online Library or from the author.

Conflict of Interest

The authors declare no conflict of interest.

Data Availability Statement

The data that support the findings of this study are available in the supplementary material of this article.

[1] A. Wang, M. He, M. A. Green, K. Sun, X. Hao, *Adv. Energy Mater.* **2023**, *13*, 2203046.

[2] S. Giraldo, Z. Jehl, M. Placidi, V. Izquierdo-Roca, A. Pérez-Rodríguez, E. Saucedo, *Adv. Mater.* **2019**, *31*, 1806692.

[3] U. Saha, M. K. Alam, *RSC Adv.* **2018**, *8*, 4905.

[4] A. P. Levanyuk, V. V. Osipov, *Sov. Phys. Usp.* **1981**, *24*, 187.

[5] J. Krustok, H. Collan, M. Yakushev, K. Hjelt, *Phys. Scr.* **1999**, *T79*, 179.

[6] J. Krustok, J. Raudoja, M. Yakushev, R. D. Pilkington, H. Collan, *Phys. Status Solidi* **1999**, *173*, 483.

[7] I. Dirnstorfer, M. Wagner, D. M. Hofmann, M. D. Lampert, F. Karg, B. K. Meyer, *Phys. Status Solidi A* **1998**, *168*, 163.

[8] M. Grossberg, P. Salu, J. Raudoja, J. Krustok, *J. Photonics Energy* **2013**, *3*, 030599.

[9] M. V. Yakushev, J. Márquez-Prieto, I. Forbes, P. R. Edwards, V. D. Zhivulko, A. V. Mudryi, J. Krustok, R. W. Martin, *J. Phys. D. Appl. Phys.* **2015**, *48*, 475109.

[10] M. V. Yakushev, M. A. Sulimov, J. Márquez-Prieto, I. Forbes, J. Krustok, P. R. Edwards, V. D. Zhivulko, O. M. Borodavchenko, A. V. Mudryi, R. W. Martin, *Sol. Energy Mater. Sol. Cells* **2017**, *168*, 69.

[11] S. Oueslati, M. Grossberg, M. Kauk-Kuusik, V. Mikli, K. Ernits, D. Meissner, J. Krustok, *Thin Solid Films* **2019**, *669*, 315.

[12] M. Grossberg, J. Krustok, C. J. Hages, D. M. Bishop, O. Gunawan, R. Scheer, S. M. Lyam, H. Hempel, S. Levcenco, T. Unold, *J. Phys. Energy* **2019**, *1*, 044002.

[13] G. Rey, A. Redinger, J. Sendler, T. P. Weiss, M. Thevenin, M. Guennou, B. El Adib, S. Siebentritt, *Appl. Phys. Lett.* **2014**, *105*, 112106.

[14] M. Grossberg, J. Krustok, J. Raudoja, T. Raadik, *Appl. Phys. Lett.* **2012**, *101*, 102102.

[15] M. Grossberg, T. Raadik, J. Raudoja, J. Krustok, *Curr. Appl. Phys.* **2014**, *14*, 447.

[16] S. Chen, J.-H. Yang, X. G. Gong, A. Walsh, S.-H. Wei, *Phys. Rev. B* **2010**, *81*, 245204.

[17] S. Chen, L.-W. Wang, A. Walsh, X. G. Gong, S.-H. Wei, *Appl. Phys. Lett.* **2012**, *101*, 223901.

[18] G. Rey, G. Larramona, S. Bourdais, C. Choné, B. Delatouche, A. Jacob, G. Dennler, S. Siebentritt, *Sol. Energy Mater. Sol. Cells* **2018**, *179*, 142.

[19] A. Jagomägi, J. Krustok, J. Raudoja, M. Grossberg, M. Danilson, M. Yakushev, *Phys. B Condens. Matter* **2003**, *337*, 369.

[20] J. Krustok, T. Raadik, R. Kaupmees, M. Grossberg, M. Kauk-Kuusik, K. Timmo, A. Mere, *J. Phys. D. Appl. Phys.* **2019**, *52*, 285102.

[21] A. Jagomägi, J. Krustok, J. Raudoja, M. Grossberg, M. Danilson, *Phys. Status Solidi* **2003**, *237*, R3.

[22] J. Márquez-Prieto, M. V. Yakushev, I. Forbes, J. Krustok, P. R. Edwards, V. D. Zhivulko, O. M. Borodavchenko, A. V. Mudryi, M. Dimitrievska, V. Izquerdo-Roca, N. M. Pearsall, R. W. Martin, *Sol. Energy Mater. Sol. Cells* **2016**, *152*, 42.

[23] S. Siebentritt, N. Papathanasiou, M. C. Lux-Steiner, *Phys. B Condens. Matter* **2006**, *376–377*, 831.

[24] J. Krustok, H. Collan, K. Hjelt, *J. Appl. Phys.* **1997**, *81*, 1442.

[25] J. Krustok, R. Kaupmees, R. Jaaniso, V. Kiisk, I. Sildos, B. Li, Y. Gong, *AIP Adv.* **2017**, *7*, 065005.

[26] Q. Li, S. J. Xu, M. H. Xie, S. Y. Tong, *Europhys. Lett.* **2005**, *71*, 994.

[27] M. Grossberg, J. Krustok, J. Raudoja, K. Timmo, M. Altosaar, T. Raadik, *Thin Solid Films* **2011**, *519*, 7403.

[28] J. Lee, E. S. Koteles, M. O. Vassell, *Phys. Rev. B* **1986**, *33*, 5512.

[29] C. Persson, R. Chen, H. Zhao, M. Kumar, D. Huang, in *Copper Zinc Tin Sulfide-Based Thin Film Solar Cells*, John Wiley & Sons Ltd, Chichester, UK, **2015**, pp. 75–105.

[30] H. Esmaielpour, V. R. Whiteside, L. C. Hirst, J. G. Tischler, C. T. Ellis, M. P. Lumb, D. V. Forbes, R. J. Walters, I. R. Sellers, *Prog. Photovoltaics Res. Appl.* **2017**, *25*, 782.

[31] G. Conibeer, S. Shrestha, S. Huang, R. Patterson, H. Xia, Y. Feng, P. Zhang, N. Gupta, M. Tayebjee, S. Smyth, Y. Liao, Z. Zhang, S. Chung, S. Lin, P. Wang, X. Dai, in Next Generation Technologies for Solar Energy Conversion V, Vol *9178* **2014**, p. 917802.

[32] Y. Rosenwaks, M. C. Hanna, D. H. Levi, D. M. Szmyd, R. K. Ahrenkiel, A. J. Nozik, *Phys. Rev. B* **1993**, *48*, 14675.

[33] C. J. Hages, A. Redinger, S. Levcenco, H. Hempel, M. J. Koeper, R. Agrawal, D. Greiner, C. A. Kaufmann, T. Unold, *Adv. Energy Mater.* **2017**, *7*, 1700167.

[34] T.-H. Cheng, P.-S. Kuo, C.-Y. Ko, C.-Y. Chen, C. W. Liu, *J. Appl. Phys.* **2009**, *105*, 106107.

[35] W. Shockley, W. T. Read, *Phys. Rev.* **1952**, *87*, 835.

[36] K. Timmo, M. Altosaar, M. Pilvet, V. Mikli, M. Grossberg, M. Danilson, T. Raadik, R. Josepson, J. Krustok, M. Kauk-Kuusik, *J. Mater. Chem. A* **2019**, *7*, 24281.

[37] J. He, L. Sun, S. Chen, Y. Chen, P. Yang, J. Chu, *J. Alloys Compd.* **2012**, *511*, 129.

[38] W. Li, K. Jiang, J. Zhang, X. Chen, Z. Hu, S. Chen, L. Sun, J. Chu, *Phys. Chem. Chem. Phys.* **2012**, *14*, 9936.